EVIDENCE FOR THE STANDARD MODEL HIGGS BOSON DECAYING TO A PHOTON AND A LOW-MASS LEPTON PAIR WITH THE ATLAS DETECTOR AT THE LHC

A. BASALAEV on behalf of the ATLAS Collaboration
Deutsches Elektronen-Synchrotron (DESY),
Notkestrasse 85, Hamburg, Germany

A search for the Higgs boson in the final state with a photon and a lepton pair (muons or electrons) with an invariant mass $m_{ll} < 30$ GeV is presented. The analysis uses a data set of pp collisions at a center-of-mass energy of 13 TeV corresponding to an integrated luminosity of 139 fb^{-1} collected with the ATLAS detector at the Large Hadron Collider. The search strategy is presented, with a focus on a novel approach for resolving close-by electron candidates. Evidence for the Higgs boson decaying to a photon and a low-mass lepton pair is found with a 3.2σ significance over the background-only hypothesis, compared to an expected significance of 2.1σ. The best-fit value of the signal strength parameter, defined as the ratio of the observed signal yield to the one expected in the Standard Model, is measured to be $\mu = 1.5 \pm 0.5$. The Higgs boson production cross-section times the $H \to \ell\ell\gamma$ branching ratio for $m_{ll} < 30$ GeV is determined to be $8.7^{+2.8}_{-2.7}$ fb.

ATL-PHYS-PROC-2021-020
05 May 2021

1 Introduction

A particle consistent with the properties of the Standard Model (SM) Higgs boson was discovered by the ATLAS and CMS collaborations in 2012 [1,2]. Since then, it has been observed independently in the $H \to \gamma\gamma$, $H \to b\bar{b}$, $H \to ZZ^{(*)} \to \ell^+\ell^-\ell^+\ell^-$, $H \to WW^{(*)} \to e\nu\mu\nu$, and $H \to \tau\tau$ decay channels. With the full data set from the second run (2015-2018) of the LHC, corresponding to 139 fb^{-1} of integrated luminosity, it becomes possible to explore rarer decay channels.

One of these channels is a decay to two leptons and a photon $H \to \ell\ell\gamma$, where $\ell = e, \mu$. With more data in the future, this three-body decay can be used to probe the CP properties of the Higgs boson [3,4]. It can also be sensitive to coupling modifications introduced by possible extensions to the SM [5]. The $H \to \ell\ell\gamma$ decay may occur in the following ways: in association with final state radiation at the tree level, through a Z boson $H \to Z\gamma \to \ell\ell\gamma$ or via a virtual photon $H \to \gamma^*\gamma \to \ell\ell\gamma$ at the one-loop level. The dominant Feynman diagrams are shown in Figure 1. For the present search [6], a requirement on the lepton pair invariant mass $m_{ll} < 30$ GeV was used; in this regime, decays predominantly occur through γ^*, and other contributions are negligible.

The CMS Collaboration reported a 95% CL upper limit on $\sigma \times \mathcal{B}$ of 4.0 times the SM prediction for the low-mass ($m_{\mu^+\mu^-} < 50$ GeV) $H \to \mu^+\mu^-\gamma$ process based on a 35.9 fb^{-1} data

set [7]. The $H \to Z\gamma \to \ell\ell\gamma$ channel was explored by the ATLAS and CMS Collaborations as well [7,8].

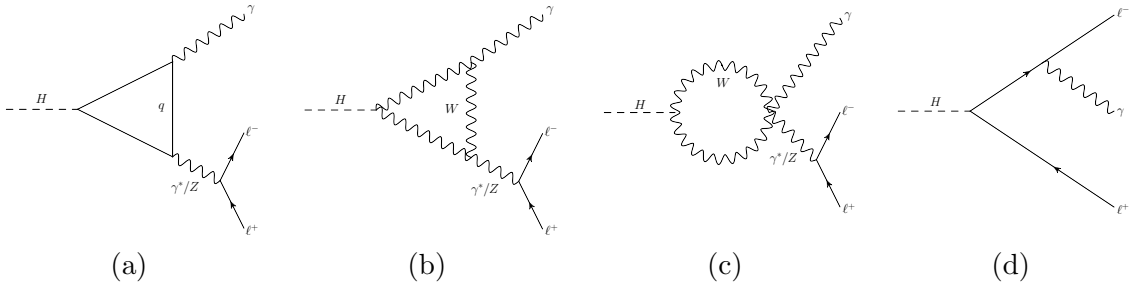

Figure 1 – dominant Feynman diagrams for the $H \to \ell\ell\gamma$ decay.

2 Object and event selection

The analysis uses 139 fb^{-1} of high-quality LHC data recorded with the ATLAS detector [9] in 2015-2018. The events in this analysis are required to pass a combination of single-lepton, dilepton, diphoton, and lepton-photon triggers. For the 2017 and 2018 data taking periods, an additional trigger was used with an upper threshold on hadronic leakage in the calorimeter, but no requirement on the width of the shower. This dedicated trigger recovered a significant fraction of low-$m_{e^+e^-}$ $H \to e^+e^-\gamma$ events, where the electrons tend to be highly collimated, resulting in reduced trigger efficiencies of traditional electron triggers.

Events with at least one γ candidate and at least two oppositely-charged electrons or muons are required. Jet candidates are used to suppress backgrounds and to select events produced through vector-boson fusion (VBF). Standard reconstruction techniques are used for muon and jet reconstruction [6]. In the standard reconstruction, (resolved) electron and photon candidates are reconstructed from the electromagnetic (EM) topoclusters and matching tracks in the ID. In events with highly collimated electrons, the corresponding EM calorimeter deposits often merge.

To recover such ee-merged events, merged electrons are reconstructed by matching two tracks to a single EM topocluster. To calibrate the energy of the merged electrons, the energy calibration for converted photons with $r = 30$ mm is used, due to their kinematic similarities. For the same reason, track requirements are applied to merged electron candidates to suppress converted photons. A multivariate discriminator is trained to separate the signal merged electron events from jet backgrounds. The identification and isolation efficiency is measured in data using a tag-and-probe method with the $Z \to \ell\ell\gamma$ events and reaches $\sim 50\%$.

The candidate events are further selected and categorized using the kinematic requirements aimed at increasing the expected significance. They are classified in three types (ordered by priority): targeting the VBF Higgs boson production mode, high-$p_{\mathrm{TThrust}}^{\ell\ell\gamma}$ [a], and low-$p_{\mathrm{TThrust}}^{\ell\ell\gamma}$ events. With ee-resolved, ee-merged and $\mu\mu$ events, this results in nine analysis categories.

3 Signal and background modelling

The signal yield is extracted from the $m_{\ell\ell\gamma}$ distribution by fitting it with parametric functions. The expected signal contribution is modelled using Monte-Carlo simulated (MC) $H \to \gamma^*\gamma$ events and fitting the $m_{\ell\ell\gamma}$ distribution with a double-sided Crystal Ball (DSCB) function, featuring a Gaussian core and asymmetric power-law tails. An illustration of signal model in the ee-merged high-$p_{\mathrm{TThrust}}^{\ell\ell\gamma}$ and ee-resolved low-$p_{\mathrm{TThrust}}^{\ell\ell\gamma}$ categories is shown in Figure 2.

The backgrounds in this analysis consist of a non-resonant component, and a much smaller resonant background from $H \to \gamma\gamma$ in the electron categories. The non-resonant background

[a] $p_{\mathrm{TThrust}}^{\ell\ell\gamma} = |\vec{p}_{\mathrm{T}}^{\,\ell\ell\gamma} \times \hat{t}|$, where $\hat{t} = (\vec{p}_{\mathrm{T}}^{\,\ell\ell} - \vec{p}_{\mathrm{T}}^{\,\gamma})/|\vec{p}_{\mathrm{T}}^{\,\ell\ell} - \vec{p}_{\mathrm{T}}^{\,\gamma}|$. This quantity is strongly correlated with the $\vec{p}_{\mathrm{T}}^{\,\ell\ell\gamma}$.

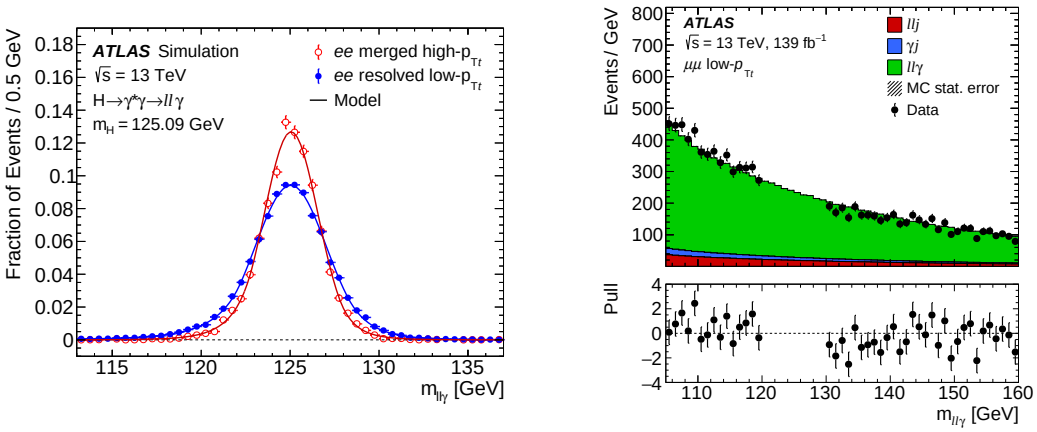

Figure 2 – left: $m_{\ell\ell\gamma}$ distribution for simulated $H \to \gamma^*\gamma$ signal [6] in the ee-merged high-$p^{\ell\ell\gamma}_{\mathrm{TThrust}}$ and ee-resolved low-$p^{\ell\ell\gamma}_{\mathrm{TThrust}}$ categories (circles), and corresponding signal models (lines); right: $m_{\ell\ell\gamma}$ distribution for data [6] (black circles) and the non-resonant background template in $\mu\mu$ low-$p^{\ell\ell\gamma}_{\mathrm{TThrust}}$ category. Contributions from different background sources are shown: the simulated $\ell\ell\gamma$ processes (green), the data-driven estimate for background with a misidentified photon ($\ell\ell j$, red) or a lepton pair (γj, blue).

is modelled by fitting a background template with a smoothly falling function in the $m_{\ell\ell\gamma}$, selecting from exponential, exponential of a second-order polynomial, or power-law functions. The functional form is chosen per category, based on the fit to a background-only template (described below) with a signal-plus-background model. Since the background template contains no signal, any fitted signal corresponds to a measurement bias (*spurious* signal); the function minimizing the spurious signal is chosen. Additionally, other criteria, such as goodness of fit, and number of degrees of freedom, are taken into account. The resonant $H \to \gamma\gamma$ background contribution is estimated using the DSCB function from the signal fit normalized to the expected $H \to \gamma\gamma$ yield.

The background template mentioned above is constructed combining the non-resonant $\ell\ell\gamma$ processes estimated using MC samples, and a smaller contribution from events with misidentified photons, electrons or muons is estimated using a data-driven technique. The data-driven estimation is based on inversion of the identification and isolation requirements, thereby forming control regions enriched in the corresponding background. The relative contribution of events with a misidentified photon amounts to 10%. The estimated fractions of events with misidentified leptons are 4% in the $\mu\mu$ low-$p^{\ell\ell\gamma}_{\mathrm{TThrust}}$ category, 2% in the ee-merged low-$p^{\ell\ell\gamma}_{\mathrm{TThrust}}$ category, and 30% in the ee-resolved low-$p^{\ell\ell\gamma}_{\mathrm{TThrust}}$ category. As an example, the background composition in the $\mu\mu$ low-$p^{\ell\ell\gamma}_{\mathrm{TThrust}}$ category is shown in Figure 2.

The resulting signal and background functions are used to construct a likelihood model, with systematic uncertainties implemented as nuisance parameters. The profile likelihood method is used to estimate the ratio of the observed signal yield to the one expected in the SM, μ, and the significance of the excess. Additionally, the $\sigma \times \mathcal{B}(H \to \ell\ell\gamma)$ for $m_{ll} < 30$ GeV is measured by multiplying $\sigma_{\mathrm{SM}} \times \mathcal{B}_{\mathrm{SM}}$ with μ and propagating the systematic uncertainties, considering only theoretical uncertainties in the acceptance, while uncertainties in the predicted cross-sections and branching ratio do not apply.

4 Results

The search is dominated by the statistical uncertainty, with systematic uncertainties amounting to just 35% of the total uncertainty on μ. Among the systematic uncertainties, the uncertainty associated with the fit bias dominates with 6.1%. The theoretical uncertainty in $\mathcal{B}_{\mathrm{SM}}(H \to \gamma^*\gamma \to \ell\ell\gamma)$ contributes with 5.8%. Other uncertainties with smaller contributions include the

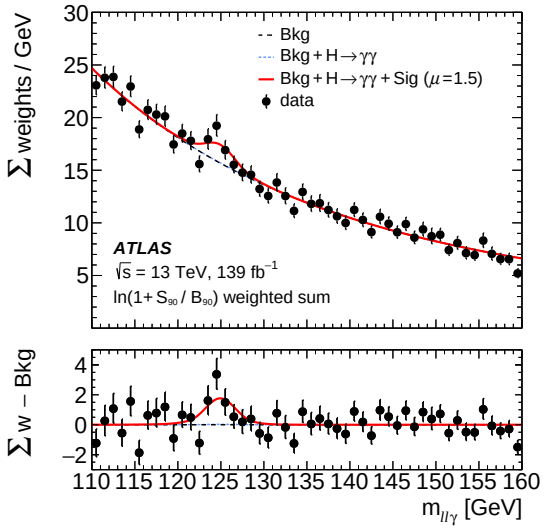

Figure 3 – $m_{\ell\ell\gamma}$ distribution [6], with every data event (black circles) reweighted by a category-dependent weight, $\ln(1 + S_{90}/B_{90})$, where S_{90} is the number of signal events in the smallest window containing 90% of the expected signal, and B_{90} is the expected number of background events in the same window. The red curve shows the combined $S + B$ model when fitting all analysis categories simultaneously, the dashed black line shows the model of the non-resonant background component and the dotted blue line denotes the sum of the non-resonant background and the resonant $H \to \gamma\gamma$ background. The bottom panel shows the residuals of the data with respect to the non-resonant background component of the $S + B$ fit.

uncertainties associated with the QCD scale and with the parton density functions, uncertainties related to identification efficiencies for the objects in the event, and the uncertainties in the energy/momentum calibration.

In Figure 3 the $m_{\ell\ell\gamma}$ distribution is shown with every data event reweighted by a category-dependent weight. The signal plus background model is also shown, as well as the background-only components: the non-resonant background and the resonant $H \to \gamma\gamma$.

An excess is found with a 3.2σ significance over the background-only hypothesis, compared to an expected significance of 2.1σ. The best-fit value of the signal strength parameter is measured to be $\mu = 1.5 \pm 0.5$. The Higgs boson production cross-section times the $H \to \ell\ell\gamma$ branching ratio for $m_{ll} < 30$ GeV is determined to be $8.7^{+2.8}_{-2.7}$ fb.

References

1. ATLAS Collaboration, *Phys. Lett.* B **716**, 1 (2012).
2. CMS Collaboration, *Phys. Lett.* B **716**, 30 (2012).
3. A. Korchin and V. Kovalchuk, *Phys. Rev.* D **88**, 036009 (2013).
4. Y. Chen, A. Falkowski, I. Low and R. Vega-Morales, *Phys. Rev.* D **90**, 113006 (2014).
5. A. Kachanovich, U. Nierste and I. Nišandžić, *Phys. Rev.* D **101**, 073003 (2020).
6. ATLAS Collaboration, arXiv: 2103.10322 [hep-ex], submitted to *Phys. Lett.* B (2021).
7. CMS Collaboration, *JHEP* **11**, 152 (2018).
8. ATLAS Collaboration, *Phys. Lett.* B **809**, 135754 (2020).
9. ATLAS Collaboration, *JINST* **3**, S08003 (2008).